





Article

Three Approaches to Low-Duty Turbo Compressor Efficiency Exploitation Evaluation

Igor Poljak ^{1,*}, Ivica Glavan ¹, Josip Orović ¹ and Vedran Mrzljak ²

¹ Maritime Department, University of Zadar, Mihovila Pavlinovića 1, 23000 Zadar, Croatia; iglavan@unizd.hr (I.G.); jorovic@unizd.hr (J.O.)

² Faculty of Engineering, University of Rijeka, Vukovarska 58, 51000 Rijeka, Croatia; vedran.mrzljak@riteh.hr

* Correspondence: ipoljak1@unizd.hr; Tel.: +385-98-613-848

Received: 27 March 2020; Accepted: 9 May 2020; Published: 13 May 2020



Abstract: This paper presents three approaches for isentropic, energy, and exergy evaluations of a low-duty liquid natural gas (LNG) vapor turbo compressor during exploitation on a conventional LNG carrier. The evaluation was conducted on the measured performance parameters under 22 various turbo compressor operating regimes. The turbo compressor performance was evaluated in the temperature span from -69 to -105 °C and during changes in the rpm of the main propulsion turbine and, consequently, the main boiler load. The results show that the highest measured turbo compressor isentropic efficiency is in agreement with the manufacturer specifications, equaling 75.23% at a main propulsion turbine rpm of 53.5. At the highest measured loads and rpm, the turbo compressor energy and exergy efficiencies reach the highest values of 57.81% and 28.51%, respectively. In each observed operating regime, the influence of the ambient temperature change on the turbo compressor exergy efficiency was investigated. At the lowest and the highest measured loads, turbo compressor energy and exergy flow streams are presented in a Sankey diagram. Techniques for cargo temperature maintenance during the ship voyage are presented, as the results show that low suction gas temperatures influence turbo compressor efficiency.

Keywords: low-duty turbo compressor; isentropic efficiency; energy analysis; exergy analysis; cargo temperature maintenance

1. Introduction

In marine propulsion systems, diesel engines prevail in the entire world's fleet [1,2]. The most common arrangement is low-speed two-stroke diesel engines being used for propulsion [3,4], while the middle- or fast-speed four-stroke diesel engines are used as auxiliary engines [5]. As such, many researchers are developing various systems that can improve the operation of these diesel engines or reduce the harmful emissions [6,7].

Gas turbines in marine propulsion systems are usually used in various combinations along with other propulsion elements [8,9], but rarely as stand-alone devices due to increased costs in comparison to other propulsion alternatives [10]. However, gas turbines are the components included in the development of new, complex, and dynamic marine propulsion systems [11,12].

The share of steam propulsion in marine propulsion is low when considering the entire world fleet, but this propulsion is still dominant on liquid natural gas (LNG) carriers due to the specificity of its operation and the transported cargo [13,14]. Notably, the proportion of propulsion alternatives for LNG carriers are continually increasing, so steam propulsion will likely lose its dominance in the near future [15].

Various auxiliary devices can be found inside each marine propulsion system (regardless whether it is based on a diesel engine, steam turbine, gas turbine, or combinations thereof), the operation

of which plays an inevitable role in the entire propulsion system operation [16–18]. Many authors have studied several auxiliary components in one or more operation regimes [19,20]. One auxiliary component inside many marine propulsion systems is a turbo compressor. In general usage, turbo compressors can be found as components of gas turbines that operate as stand-alone devices [21–23] or as a part of various complex systems [24–26]. They are also found in many heat-recovery systems that, in most cases, produce additional mechanical power [27,28]. The literature provides various other examples of turbo compressor usage [29,30].

Engineers and scientists agree that proper turbo compressor construction and maintaining its desired operation is usually a notable challenge [31] due to turbo compressors increasing the gaseous operating medium pressure and delivering it from lower to higher pressure. This operation principle is opposed to natural fluid flow (from higher to lower pressure) [32]. This operation produces many difficulties and problems during the operation of any turbo compressor [33].

Inside the propulsion systems of LNG carriers, turbo compressors are used to increase the pressure of boil off gas (BOG) from the cargo tanks and deliver it to main propulsion element inside the system (dual fuel internal combustion engines or steam generators). LNG carriers can also have a system for BOG re-liquefaction [34,35] or a combination of re-liquefaction and compression to the main propulsion element. Studies about BOG turbo compressors, especially under various loads and/or in exploitation, are rare in the scientific and professional literature. One recent study examined the two-stage BOG turbo compressor that delivers evaporated gas from cargo tanks to a dual fuel main internal combustion engine [36]. The mentioned research and two-stage axial turbo compressor analysis were based on measured data from exploitation under various turbo compressor loads. We did not find any other detailed investigation of the same or similar BOG turbo compressors in the literature, which was the main motivation for the research presented in this paper.

In this study, we conducted isentropic, energy, and exergy analysis of a low-duty BOG single-stage radial turbo compressor. The turbo compressor takes evaporated gas from the LNG carrier cargo tanks, increases its pressure, and delivers it into steam generators. In steam generators, evaporated gas is burned and superheated steam is produced, which is used for the main and all auxiliary steam turbine driving. The low-duty BOG turbo compressor plays an important role in maintaining the operating parameters of the cargo tanks for the analyzed LNG carrier [37]. The change in low-duty BOG turbo compressor load influences the vaporized gas mass flow rate delivered to the steam generators, consequentially causing changes in turbo compressor efficiency and losses. Based on the measured results from experiments, a low-duty BOG turbo compressor was analyzed under various operating regimes. The results of this analysis will be necessary for further research and possible optimization of the observed turbo compressor.

The usage of BOG as a fuel in comparison to other conventional fuels emits fewer harmful emissions; BOG emits almost no sulfur oxides (SO_x) or particulate matter (PM), while carbon dioxide (CO_2) and nitrogen oxides (NO_x) emissions can be notably reduced [38,39]. This is an additional reason why analyzing BOG turbo compressor operation is important.

2. Process Flow and Low-Duty Turbo Compressor Description

Low-duty turbo compressors are used on conventional LNG tankers for supplying the main boilers with evaporated natural gas from the cargo tanks, as shown in Figure 1. Liquefied natural gas evaporates from the cargo tank, then the low-duty turbo compressor sucks the gas from the cargo tank (suction pressure p_1 , suction temperature t_1), passing through a moisture separator, and delivering the evaporated gas to the gas heater (delivery pressure p_2 , delivery temperature t_2). Then, the heated gas is fed to the main boiler. In the main boiler, water evaporates and then is used for the propulsion of the main turbine, turbo generators, main feed pump drive, and for services. After the low-duty turbo compressor, the natural gas is heated as it is still at a low temperature. The low temperature of the gas changes the gas calorific value and density, and this gas is hard to control for normal combustion

inside the boiler. As such, the system is fitted with a gas heater that heats the gas to within 30 to 40 °C before entering the main boiler.

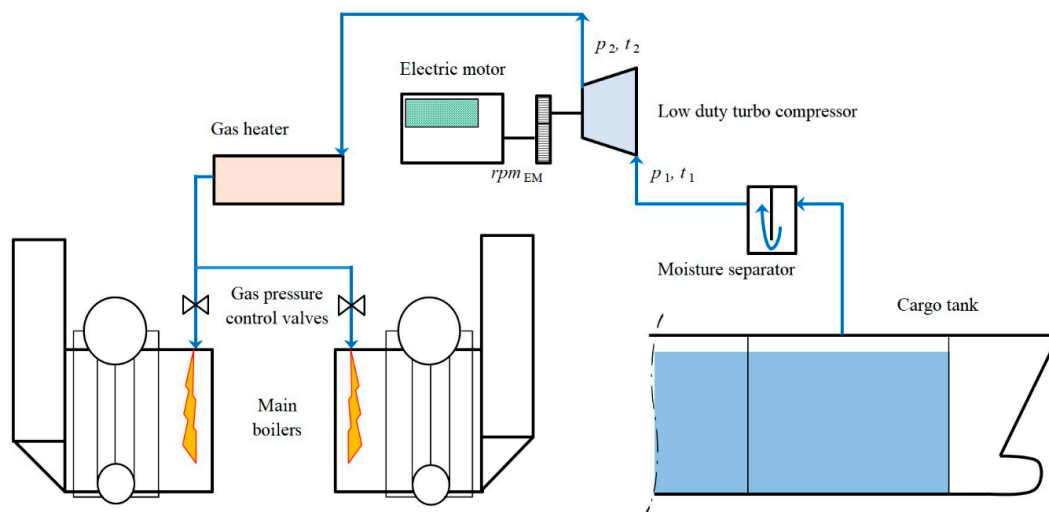


Figure 1. Natural gas supply with low-duty turbo compressor on a conventional liquid natural gas (LNG) carrier.

The low-duty gas turbo compressor is a single-stage centrifugal turbo compressor with a dual delivery control mode. The fuel oil demand signal from the main boilers controls the operation of the low-duty turbo compressor. The signal is split into two operating modes. In the low operating delivery mode, the low-duty turbo compressor inlet guides the vane position. The control of the inlet guide vanes ranges from -30 to $+80$ degrees. In high operating delivery mode, the low-duty turbo compressor controls the electric motor speed, which is increased and decreased using a variable frequency control drive. The electric motor control ranges from 30 to 60 Hz or 1793 to 3585 rpm [40]. The turbo compressor speed is transmitted to the gear box, where it is converted to the range of 12,000 to 24,000 rpm. The gear box consists of two helical gears that are supported by bearings. At the drive shaft, the gear box is attached gearing for the main lube oil pump, which feeds the oil to the bearings and to the drive gear. A seal system is provided between the gear shaft bearing and the compressor wheel. The shaft seal prevents oil from entering the process stream and from freezing inside the compressor (Figure 2).

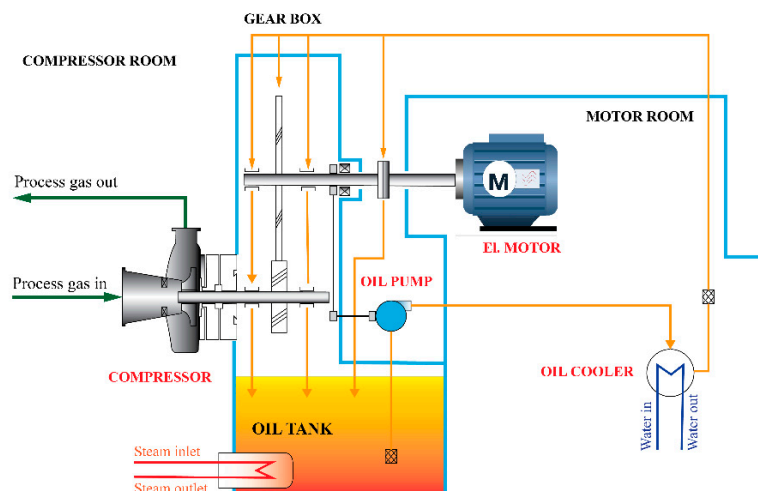


Figure 2. Scheme of low-duty turbo compressor with electric motor and reduction gear.

The low-duty turbo compressor is equipped with a bypass valve, which protects the equipment from surges in the case of a sudden stop in gas delivery or increased line pressure, during which gas may flow back to the rotor. This would cause a high load on the bearings, high vibration, and rapid rise in the internal temperature of the gas. The principal characteristics of the low-duty turbo compressor are listed in Table 1.

Table 1. Turbo compressor design data [41].

Parameter.	Unit	Natural Gas Type 1	Natural Gas Type 2
Molecular weight	kg/kmol	18.64	18.44
Flow	Nm ³ /h	8500	4000
Inlet pressure	kPa	103	103
Inlet temperature	°C	−40	−140
Outlet pressure	kPa	200	200
Shaft speed	rpm	24,000	17,000
Isentropic efficiency	%	77%	-

3. Measuring Equipment and Measured Results

The measured results were collected from the vessel's departure from the port. Measurement commenced at dead slow ahead of the main engine and as the engine load increased until 83 rpm. Data were collected for the 22 different running points of the low-duty turbo compressor. The measurements included gas inlet and outlet temperatures, gas inlet and outlet pressures, and the mass flow rate of the main boiler. Two mirror-oriented main boilers that consume delivered gas were placed on the vessel. The measured results are listed in Table 2 and measurement equipment was described in previous studies [42–45]. The LNG cargo consists of the following components by mass ratio [46]: CH₄ (0.87955), C₂H₆ (0.08328), C₃H₈ (0.02056), C₄H_{10i} (0.00272), C₄H_{10n} (0.00400), and N₂ (0.00989).

Table 2. Measured values of natural gas before and after low-duty turbo compressor.

Main Propulsion Shaft Speed (rpm)	Gas Temperature (°C)	Gas Pressure in (MPa)	Gas Temperature Out (°C)	Gas Pressure Out (MPa)	Mass Flow (kg/h)
25.6	−70	0.1097	−55	0.1260	3332
34.3	−69	0.1096	−55	0.1261	3346
41.8	−72	0.1098	−57	0.1255	3285
53.5	−72	0.1094	−57	0.1370	3942
61.5	−89	0.1110	−75	0.1274	4270
63.6	−89	0.1111	−75	0.1290	4453
65.1	−90	0.1108	−75	0.1312	4619
66.1	−90	0.1106	−76	0.1328	4792
67.7	−91	0.1104	−76	0.1350	4849
68.7	−92	0.1102	−77	0.1364	5120
69.5	−92	0.1099	−77	0.1373	5207
70.4	−93	0.1098	−77	0.1392	5295
71.0	−93	0.1099	−77	0.1397	5210
73.1	−95	0.1094	−76	0.1461	5559
74.6	−96	0.1089	−76	0.1503	5922
76.6	−97	0.1084	−74	0.1657	6324
78.4	−98	0.1079	−73	0.1628	6526
79.5	−100	0.1078	−73	0.1670	6773
80.4	−101	0.1075	−73	0.1718	6941
81.5	−102	0.1074	−73	0.1730	6868
82.9	−104	0.1071	−74	0.1777	7057
83.0	−105	0.1071	−74	0.1783	7103

The measured values for the amperage, frequency, and the power factor were collected at the high voltage control breaker, which monitors current, frequency, and power factor value at the inlet of the electric motor (Table 3). The measured power factor was the same within the entire measured range, $\varphi = 0.9$. The electric motor speed was measured from the HIMAP M, which is a multifunctional digital protection relay with measuring functions, [47]. The maximal electric motor speed was 3585 rpm

and the turbo compressor running range is 12,000 to 24,000 rpm, as per the manufacturer. From that information, we calculated the running speed of the turbo compressor using the measured electric motor speed and following relation:

$$C_{rpm} = \frac{EM_{rpm} \cdot 24000}{3585}. \quad (1)$$

Table 3. Measured values for current, frequency and power factor.

Main Propulsion Shaft Speed (rpm)	Amperage (A)	Frequency (Hz)	Electric Motor Speed (rpm)	Low-Duty Turbo Compressor Speed (rpm)
25.6	311	29.8	1790	11,983
34.3	311	29.8	1789	11,977
41.8	311	29.8	1791	11,990
53.5	323	30.7	1843	12,338
61.5	315	29.8	1790	11,983
63.6	316	29.8	1790	11,983
65.1	319	29.8	1790	11,983
66.1	320	29.8	1790	11,983
67.7	322	29.8	1790	11,983
68.7	324	29.8	1790	11,983
69.5	326	29.8	1791	11,990
70.4	329	30.3	1816	12,157
71.0	330	30.3	1817	12,164
73.1	340	32.9	1976	13,229
74.6	349	35.0	2099	14,052
76.6	363	37.5	2249	15,056
78.4	371	39.6	2373	15,886
79.5	375	40.6	2435	16,301
80.4	386	42.1	2523	16,890
81.5	388	42.2	2532	16,951
82.9	395	43.4	2602	17,419
83.0	396	43.2	2594	17,366

4. Energy and Exergy Analysis of the Low-Duty Turbo Compressor

We analyzed the energy of the low-duty turbo compressor using two standard but different approaches. The first approach was isentropic analysis and the second was energy analysis. The isentropic and energy of the turbo compressor were analyzed according to the following set of equations [48–51]. In the steady state system, the identity of the matter within the control volume changes continuously, but the total amount present at any instant remains constant:

$$\frac{dm}{dt} = 0. \quad (2)$$

Then, the total incoming and outgoing rates of mass flow are equal:

$$\sum_{IN} m = \sum_{OUT} m. \quad (3)$$

As in the steady state, the mass flow rate and energy transfer are constant with time. Then:

$$\frac{dE}{dt} = 0. \quad (4)$$

For one inlet and one exit control volume with one-dimensional flow, the energy rate balance is:

$$\frac{dE}{dt} = Q - P + \sum_{IN} m \cdot \left(h + \frac{\bar{v}^2}{2} + g \cdot z \right) - \sum_{OUT} m \cdot \left(h + \frac{\bar{v}^2}{2} + g \cdot z \right). \quad (5)$$

In general, the energy efficiency is a ratio of useful and used energy rates in the process:

$$\eta_I = \frac{E_{OUT}}{E_{IN}} = 1 - \frac{El}{E_{IN}}. \quad (6)$$

The isentropic process efficiency of the low-duty turbo compressor is given by:

$$\eta_{IS} = \frac{P_{IS}}{P_{CA}} = \frac{m \cdot (h_{IS} - h_1)}{m \cdot (h_2 - h_1)} = \frac{(h_{IS} - h_1)}{(h_2 - h_1)} \quad (7)$$

The efficiency, which includes isentropic efficiency, electric motor efficiency, and mechanical loss, is calculated as:

$$\eta = \eta_{IS} \cdot \eta_{EM} \cdot \eta_{ME}. \quad (8)$$

For the calculation of all energy losses for the low-duty turbo compressor, which are from the gear box, seals and electric motor, the energy balance rate is set as per [52–54]:

$$P_{EM} + m \cdot h_1 = m \cdot h_2 + El. \quad (9)$$

The energy rate loss is calculated by:

$$El = P_{EM} + m \cdot (h_1 - h_2). \quad (10)$$

The energy efficiency is:

$$\eta_I = \frac{P_{CA}}{P_{EM}} = 1 - \frac{El}{P_{EM}} = 1 - \frac{P_{EM} + m \cdot (h_2 - h_1)}{P_{EM}} = \frac{m \cdot (h_2 - h_1)}{P_{EM}}. \quad (11)$$

The required electrical power was calculated from the measured equipment as follows: the frequency of an alternating voltage or current is related to the angular velocity of a rotating coil. The units of angular velocity are radians per second, and 2π radians (57.3 degrees) is a full revolution. One cycle of the sine wave is generated when the coil rotates 2π radians. Equation (12) describes the mathematical relationship between frequency f and the angular velocity ω in an alternating current (AC) circuit [55]:

$$\omega = 2 \cdot \pi \cdot f. \quad (12)$$

The maximum induced voltage is called the peak voltage E_p . If t is the time in which the coil turns through the angle θ , then the angular velocity ω of the coil is equal to θ/t . Equation (13) is the mathematical representation of the angular velocity:

$$\theta = \omega \cdot t. \quad (13)$$

The mathematical representation of the voltage associated with any particular orientation of the coil is:

$$e = EMF_{\max} \cdot \sin(\theta). \quad (14)$$

Substitution of Equation (13) into Equation (14) gives Equation (15), which is a mathematical representation of the relationship between the voltage induced, the maximum voltage, and the angular velocity, and is equal to the output of an AC generator:

$$e = EMF_{\max} \cdot \sin(\omega t). \quad (15)$$

We calculated the electric motor power according to the following formula, which was drawn from the literature [56,57]:

$$P_{EM} = \frac{\sqrt{3} \cdot I \cdot U \cdot \cos(\varphi)}{1000}. \quad (16)$$

Further substitution of Equation (15) into Equation (16) yields:

$$P_{EM} = \frac{\sqrt{3} \cdot I \cdot EMF_{\max} \cdot \sin(\omega t) \cdot \cos(\varphi)}{1000}. \quad (17)$$

The low-duty turbo compressor exergy was evaluated according to the literature [58–63]. The exergy rate balance of steady flow systems is:

$$\frac{dE}{dt} = \sum \left(1 - \frac{T_0}{T}\right) \cdot Q - P + \sum_{IN} m \cdot ex - \sum_{OUT} m \cdot ex - Exd. \quad (18)$$

where ex is the specific exergy, which is expressed as:

$$ex = h - h_0 - T_0 \cdot (s - s_0). \quad (19)$$

The exergy balance rate of the low-duty turbo compressor is:

$$P_{EM} + m \cdot ex_1 = m \cdot ex_2 + Exd. \quad (20)$$

The exergy destruction rate of the low-duty turbo compressor is calculated by:

$$Exd = P_{EM} + m \cdot (ex_1 - ex_2). \quad (21)$$

The exergy efficiency of the low-duty turbo compressor is:

$$\eta_{II} = \frac{Ex_{out}}{Ex_{in}} = 1 - \frac{Exd}{Ex_{in}} = 1 - \frac{P_{EM} + m \cdot (ex_1 - ex_2)}{P_{EM}} = \frac{m \cdot (ex_1 - ex_2)}{P_{EM}}. \quad (22)$$

The reference value for exergy calculation is 25 °C and 0.1 MPa according to [64,65].

5. Low-Duty Turbo Compressor Isentropic, Energy, and Exergy Analysis

For the low-duty turbo compressor analysis, we compared three different approaches to the efficiency calculation and analyzed their results.

Two running points of the low-duty turbo compressor are given in the h - s diagram in Figure 3. The actual compression of the gas in the low-duty turbo compressor is 1-2 and the isentropic compression is 1-2_{IS}. The first compression was recorded at dead slow ahead and the second running point of the low-duty turbo compressor was 3-4 and isentropic 3-4_{IS}, which was taken as the last measured point. Figure 3 shows that the angle at first compression from 1-2 related to 1-2_{IS} is wider than the isentropic turbo compression in the case of compression from 3-4 related to 3-4_{IS}. The wider angle distance from the isentropic compression line is related to the higher entropy generation at lower loads of the low-duty turbo compressor compared to the higher turbo compressor load. Figure 3 also shows that the second running point of the low-duty turbo compressor is not in the saturated area, but is located in the two-phase zone where $x \approx 0.992$. As flying LNG drops may damage the turbo compressor, so a

moisture separator is fixed before the low-duty turbo compressor in which LNG droplets are separated from the gas phase of the LNG.

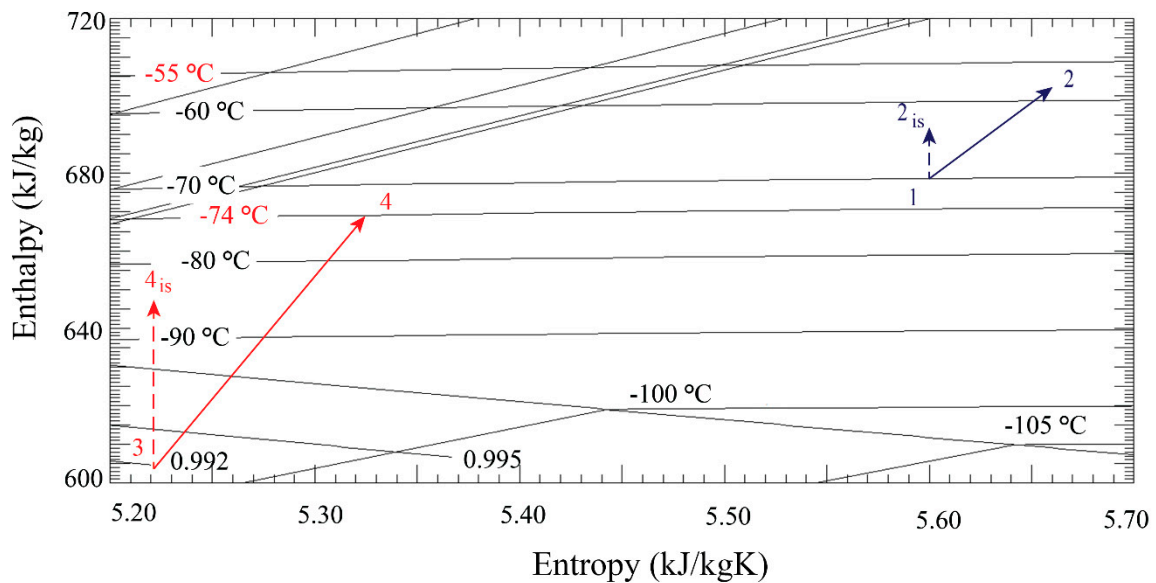


Figure 3. Low-duty turbo compressor, two running points, the lowest measured load (1-2), and the highest measured load (3-4).

Entropy generation in the actual process occurs, but is not incorporated in the isentropic efficiency of the low-duty turbo compressor. Isentropic efficiency was evaluated as per Equation (7).

Figure 4 compares the analysis of the energy loss with the low-duty turbo compressor speed. Turbo compressor speed is directly related to boiler load with its output at the main propulsion shaft. The energy loss in the lower running zones ranged from 93 to 95 kW and then decreased until 70.4 rpm, reaching 83 kW. In that range, the turbo compressor speed is almost at its minimum of around 12,000 rpm. Increasing the turbo compressor speed increases the energy loss, which peaks at 80.4 rpm, at up to 100 kW. After that point, increasing the turbo compressor speed to more than 17,000 rpm reduces the energy loss of the turbo compressor.

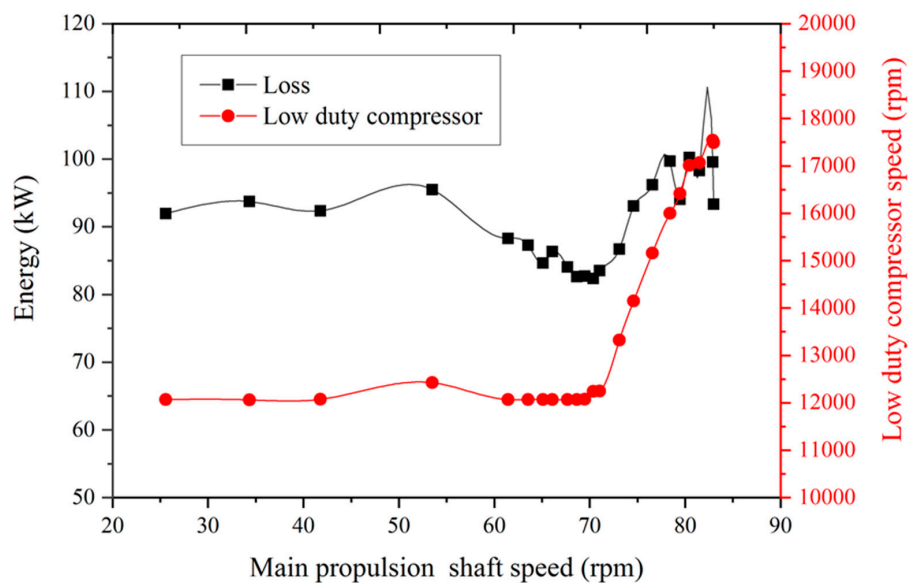


Figure 4. Energy loss vs. turbo compressor speed.

The turbo compressor operation is led by the main boilers' gas management control. The gas delivery to the main boilers is controlled by the turbo compressor inlet guide vanes' (IGV) position, turbo compressor speed, and the main boiler gas pressure control valves. The main boiler's gas pressure control valves are calibrated with normal delivery of the turbo compressor and are opened 75% of their full extent. If the main boilers change load operation, the gas pressure control valves open more to ensure the main boilers receive enough gas with changes in turbo compressor IGV position and speed. If the load on the main boilers drops down, the gas pressure control valves close to less than 75% and reduce amount of the gas to the main boilers. At the same time, the turbo compressor reduces speed and changes the IGV position if required. Figure 4 shows that the main boiler does not require a significant speed change in the turbo compressor up to 70 rpm; gas delivery is controlled to the main boilers with the IGV operation and the position of the gas pressure control valves. The burning mode at that time is a dual fuel mode with fuel oil at a minimum and the rest of the power provided by gas burning. The highest measured rpm of the turbo compressor was recorded at the two last measured points, which was about 73% of the turbo compressor's full speed. The turbo compressor speed and delivery are also related to the gas temperature. At lower temperatures, a lower speed of the turbo compressor wheel is required for pressurizing the higher density gas.

The isentropic efficiency and energy efficiency are compared in Figure 5. The highest isentropic efficiency was achieved in the mid-operation range at 53.5 rpm, when the turbo compressor speed was 12,338 rpm. The isentropic efficiency at that point was 75.23%, which is very close to the manufacturer's value of 77%, but for different temperature and running conditions. Although we measured the highest isentropic efficiency of the turbo compressor at that point, this point is not a significant point, as measured results were not grouped. The gap between half ahead and the full ahead command was 11.7 rpm, when the main boiler steam flow increases for the main propulsion turbine, while the dump steam line is closed. This event caused a surge in the turbo compressor delivery gas flow to the main boilers by variation in speed, IGV operation of the turbo compressor, and main boiler's gas pressure control valves. As the data were measured every two seconds, we expected the real measuring and exploitation conditions to deviate from the ideal manufacturer's values due to steam plant dynamics. More accurate measurement results could have been recorded if we had more time to observe that point, but due to commercial reasons, this was unfortunately not possible.

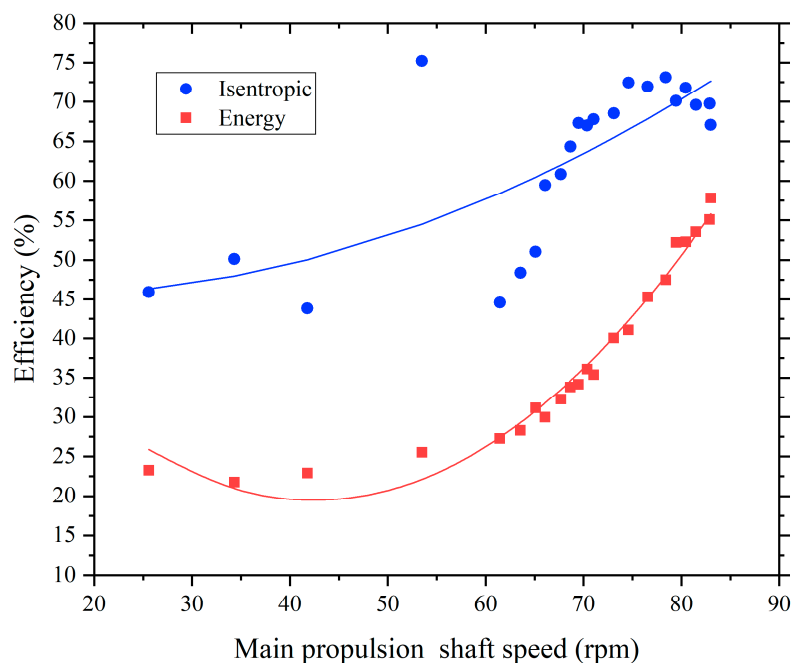


Figure 5. Isentropic and energy efficiency.

The typical parabolic shape of the isentropic efficiency curves started from 66.1 until 83 rpm, which agrees with the values in the literature [66,67]. The average isentropic efficiency of the whole measured range was 62.73%, and the highest efficiency at the grouped measured points was 73.14%.

The main difference between the isentropic and energy efficiency methods is that energy efficiency evaluates the whole unit with electric motor, gear, and seal losses, but not the turbo compressor only. Comparing Figures 4 and 5, it may be seen that the lowest energy loss is related closer to the highest isentropic efficiency of the turbo compressor but to the highest energy efficiency of the turbo compressor unit. According to the energy analysis, efficiency at 53.5 rpm is not the highest. The highest energy efficiency was found at the last measured point, 57.81%. The average energy efficiency was in the range of 21.78% to 57.81%, with a total average of 37.57%.

Energy loss is shown in a Sankey diagram in Figure 6 [68]. Two running points are presented here: at the beginning and the end of the measurement. Electric energy brought to the process in kW is compared with the actual compression process, electric motor loss, and energy loss. Accordingly, for the first running point, the electric motor loss was 10%, the energy loss was 69.07%, and 20.93% of the energy was usefully consumed. At the last running point, 10% was the electric motor loss, 37.97% was the energy loss, and 52.02% was usefully consumed energy. The Sankey diagram shows that the share of energy loss did not increase much with the increase in compression energy requirements, which positively affected the energy efficiency. As the measured power factor was the same throughout the measurements, we found that the electric motor loss was proportional to the increase in electric motor power.

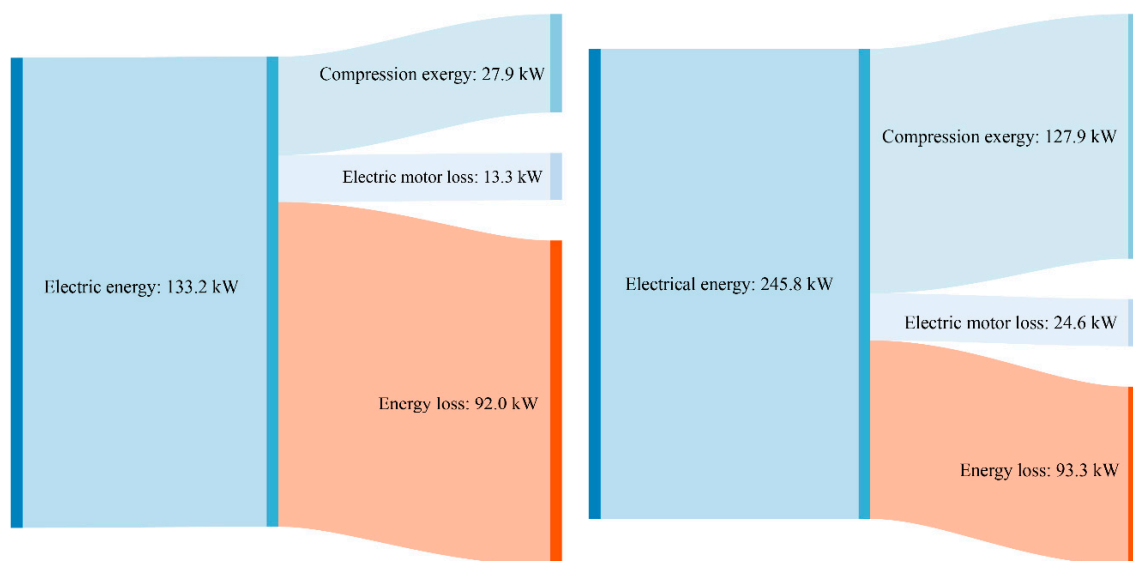


Figure 6. Sankey energy flow diagram for the lowest and highest measured turbo compressor load.

A comparison of the energy loss and exergy destruction is provided in Figure 7. Exergy destruction was more evenly distributed in the lower running zones compared to energy loss. The exergy destruction was 105 kW in that range and varied by about 10 kW, which was higher than to energy loss, which decreased from 92 kW in the beginning of the measured range to 82.4 kW in the mid-running period. As the load of the turbo compressor increased, exergy destruction constantly increased compared to the energy loss, with the highest value of about 158 kW at the last measured point. This is 58% higher than the energy loss, which peaked at 100.2 kW. The trend with increasing turbo compressor speed above 17,000 rpm was not observed for reducing the exergy destruction, which was the case for the energy losses.

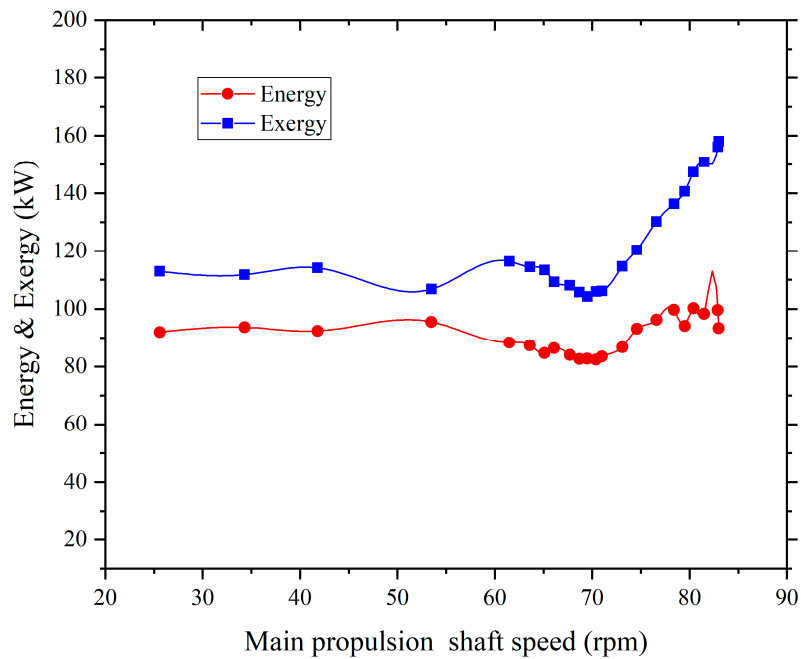


Figure 7. Energy loss and exergy destruction.

Exergy destruction and exergy of compression are shown in a Sankey diagram in Figure 8 [68]. The same two running points were considered as in the Sankey energy flow. Electric energy brought to the process in kW was compared with the actual exergy required for the compression process, electric motor destruction, and exergy destruction. In the first running point, the electric motor exergy destroyed 10%; the rest remained for the exergy destruction of the first running point, which was 84.83%. The useful process exergy consumption was only 5.17%. At the last measured point, 10% was again the electric motor exergy destruction, 64.34% was exergy destruction, and 25.66% was usefully consumed exergy. According to the Sankey diagram, the share of exergy destruction increased with increases in compression exergy requirements, which is different compared to that of the energy losses.

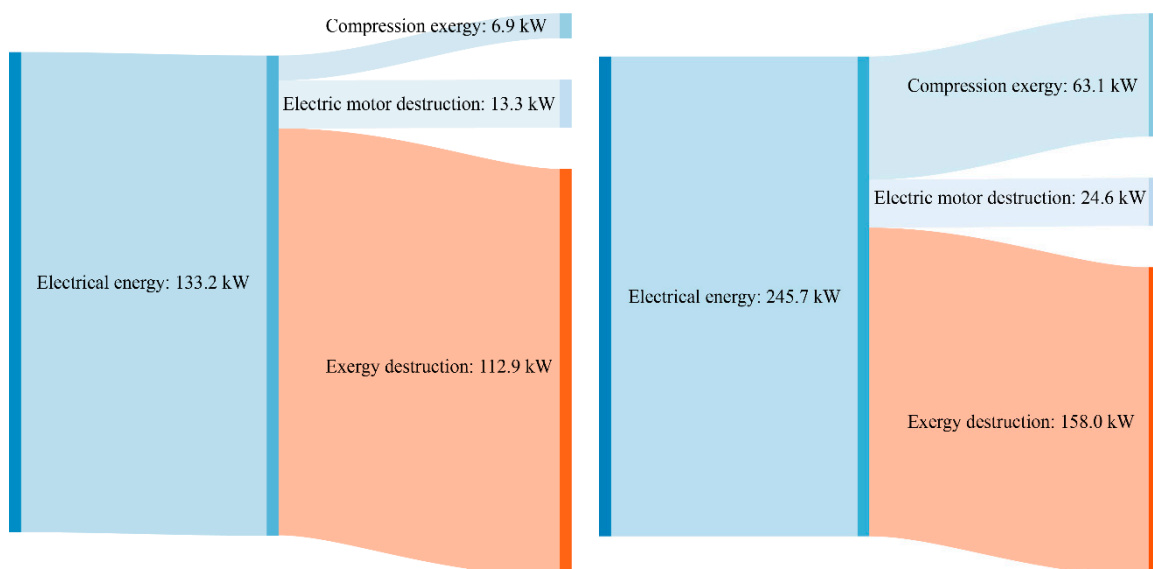


Figure 8. Sankey exergy flow diagram for the lowest and highest measured turbo compressor loads.

Figure 9 compares the isentropic and exergy efficiencies of the low-duty turbo compressor. Exergy efficiency analysis considered the whole unit, similar to the energy efficiency analysis. According to the exergy efficiency analysis, the low-duty turbo compressor efficiency in the lower running zones is 7.6% on average, with the lowest efficiency of only 4.07%, which is very poor. In the mid-running zone, the average exergy efficiency was 16.01%, and 27.87% in the upper running zone, with a peak at 29.87%, which is below 30%. In the fourth running point, the exergy efficiency increase was slightly higher compared with the energy analysis; the exergy analysis showed a more similar trend to isentropic efficiency, but with different results. The fourth measured point was related to the full ahead command to the engine telegraph, which results in higher mass flow through the turbo compressor with fully opened inlet guide vanes and slightly increased turbo compressor speed at 12,338 rpm.

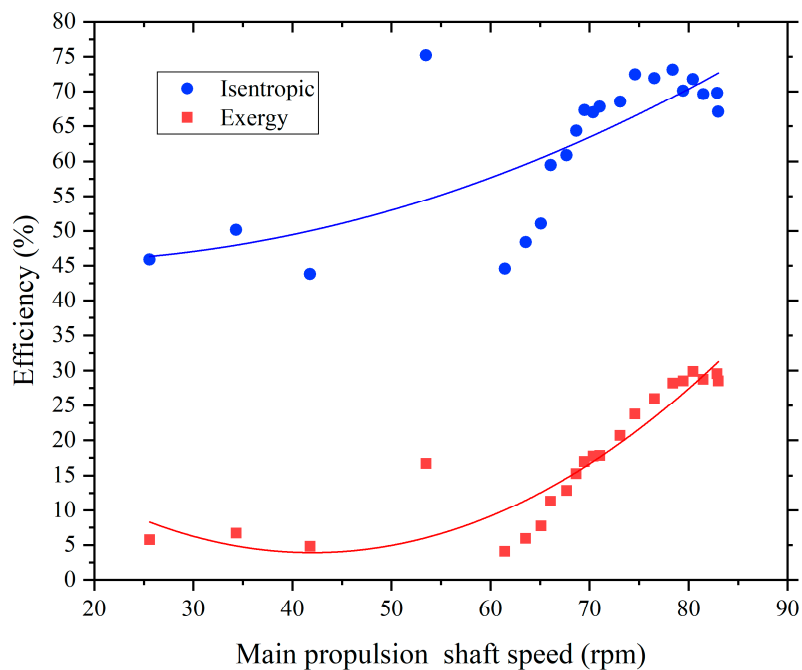


Figure 9. Isentropic and exergy efficiency.

The effects of surrounding temperature change on exergy efficiency and its sensitivity are evaluated in Figure 10. The temperature range for the evaluation of the low-duty turbo compressor exergy efficiency was 0 to 50 °C. This zone was selected because the vessel spends most of the sailing time in that temperature range. In the lower running zones of the low-duty turbo compressor, exergy efficiency decreases evenly for each 10 °C by about 0.6%. In the upper running zones, the low-duty turbo compressor is more sensitive to temperature changes; the exergy efficiency decreases in that zone by about 1%. The total average exergy efficiency deterioration with surrounding temperature changes was an average of 3.34%; the turbo compressor was more sensitive to surrounding temperature change in the higher running zones and with lower temperature gas. The ideal for this type is higher unit exergy efficiency if the vessel is sailing in colder areas, so the turbo compressor will have to destroy less exergy for the same task.

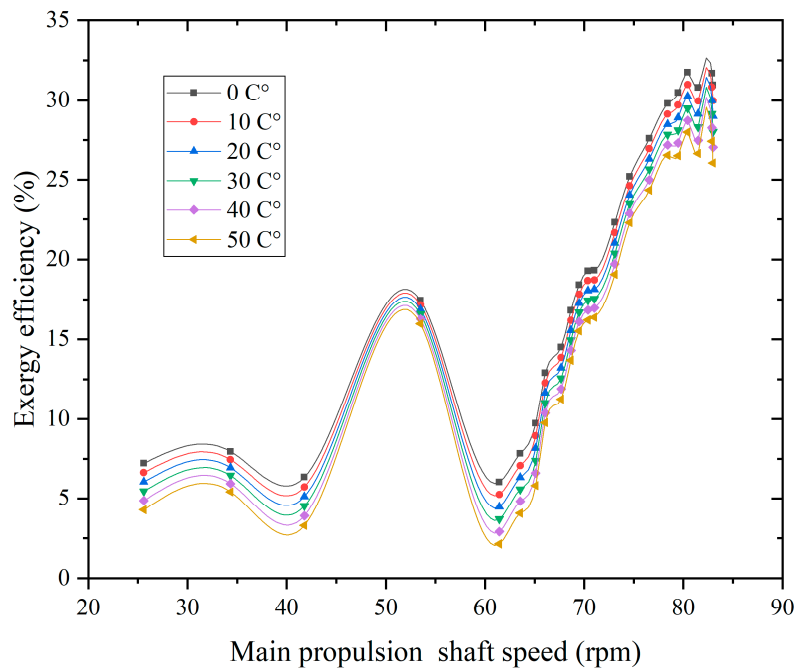


Figure 10. Exergy efficiency with surrounding temperature change.

6. Low-Duty Turbo Compressor Mass Flow and Tank Equilibrium Pressure Maintained during a Voyage

In the mixtures of various gases, equilibrium exists at specific temperatures and pressures. Changes in the temperature or the pressure move the gas mixture from one equilibrium state to another. In this part, we estimated the tank temperature during maneuvering and when sailing with the assumption that the mass flow rate of the main boiler is constant all the way to the discharging port for a 15-day voyage.

The equation of the state for the gas component, assuming that the component is at the same volume and temperature, of the mixture is [69–71]:

$$p_i \cdot v = Z_i \cdot R \cdot T. \tag{23}$$

The specific volume is:

$$v = \frac{V}{m}. \tag{24}$$

Substitution of Equation (23) into Equation (24) gives:

$$p_i \cdot V = Z_i \cdot m \cdot R \cdot T. \tag{25}$$

As per an additive pressure rule known as Dalton’s model, the gas mixture occupying volume V at temperature T can be expressed as the sum of the pressures exerted by the individual components:

$$p_m = \sum_{i=1}^j p_i(T_m, V_m). \tag{26}$$

Substitution of Equation (25) into (26) gives:

$$Z = \sum_{i=1}^j y_i \cdot Z_i|_{T_m, V_m}. \tag{27}$$

Approximation of compressibility factor Z and temperature T by the variation of the gas mixture equilibrium pressure from 0.105 to 0.125 MPa according to Equation (22) gives the following polynomials:

$$Zf(p) = 0.762860 \cdot p^3 - 2.191443 \cdot p^2 + 0.638980 \cdot p + 0.877609, \quad (28)$$

$$R^2 = 0.999317,$$

$$Tf(p) = -392.45 \cdot p^2 + 205.53 \cdot p - 179.66, \quad (29)$$

$$R^2 = 1.000000.$$

Finally, collecting the partial components in Equations (26)–(29) to a real mixture equation of state at equilibrium pressure gives:

$$p \cdot V = Zf(p) \cdot m \cdot R \cdot Tf(p). \quad (30)$$

In an LNG tanker, cargo tanks are filled up to 98% as required according to the Lloyd register, which is the safety margin to delay cargo tank overflowing in the case of fire [72]. However, some administrations will allow for a greater tank volume, typically 98.5%, which considers the expected boil-off of vapors from the cargo tanks during the loaded voyage, [73]. Membrane cargo tanks for a 150,000 m³ LNG carrier are built for an average daily vaporization rate of 0.15% of the total cargo [74,75]. The measured cargo tank pressure after loading and before starting the low-duty turbo compressor was 0.1097 MPa. The average time from dead slow ahead to fully maneuvering was divided into three one-hour-long steps. The last measurement of the main boiler was recorded as the constant consumption rate of the main boiler for the next 15 days of the assumed voyage. According to the given assumptions, we calculated 6559.4 kg/h available gas in the cargo tanks with 2% available volume, as shown in Figure 11. As the voyage continues, there is more available space in the cargo tanks due to gas consumption by the main boiler. As the main boilers are consuming more gas than available in the cargo tanks, one part of the gas must be evaporated in the LNG vaporizer, which has to simultaneously compensate for the lack of gas in the tanks and balance cargo tank pressure. In the case of the steady model as presented here, the vaporizer must vaporize an additional 3045 kg/h of LNG to maintain the cargo pressure in the tank. As the cargo tank pressure and liquid temperature are correlated, the cargo temperature is maintained for the entire voyage at about -161.92 to -161.85 °C. The only disturbance in the equilibrium was noticed during maneuvering, where the cargo tank pressure was not steady but dependent on the load change in the boiler. The total consumption of the cargo for the voyage with this setup was 2554 MT of LNG.

The extension of this work is to collect a few real laden passages data and to perform voyage optimization with respect to the ship speed and the obtained results of the low-duty turbo compressor exergy efficiency running zones from this analysis. According to the received results, power savings with a variety of low-duty compressor running modes will be compared.

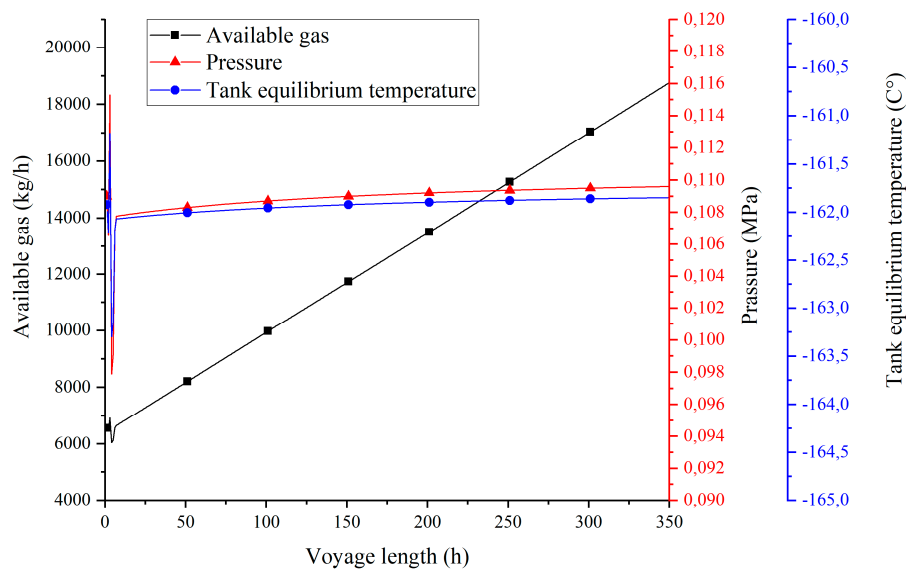


Figure 11. Cargo equilibrium temperature maintenance for the voyage.

7. Conclusions

In this study, we analyzed the isentropic, energy, and exergy efficiency of a low-duty liquid natural gas (LNG) vapor turbo compressor during exploitation on a conventional LNG carrier. Isentropic analysis is widely used for the industrial estimation of turbo compressor efficiency. Isentropic efficiency only considers turbo compressor efficiency. The evaluation of the whole machinery is more complex and requires separate mechanical efficiency measurements. If calculated according to Equation (8) with an estimated mechanical efficiency of 0.98 and measured electric motor efficiency of 0.9, without complex measurements of the mechanical seal efficiency, the calculated efficiency is lower compared to the isentropic efficiency for the whole measurement range, which is about 13.38%. As Equations (7) and (8) are widely used for the evaluation of similar machines, this may lead to incorrect assumptions about the real efficiency of the analyzed machinery. The measured results were very close to the manufacturer's reported efficiency, and the best isentropic efficiency of the typical isentropic curve was 73.14%, which agrees with the manufacturer's evaluation.

Energy efficiency evaluations are applicable for the analysis of the turbo compressor and the whole machinery, as they require fewer measurements and directly evaluate the whole machinery by measuring the required power consumption of the electric motor, meaning that no assumptions are required. The energy efficiency of the low-duty turbo compressor with its motor, gear box, and mechanical seal is lower than the isentropic efficiency, with the best evaluation being 57.81%.

Exergy efficiency evaluation is also applicable for the analysis of the turbo compressor and the whole machinery as it requires fewer measurements due to being related to power consumption and the useful exergy of the system. As the exergy efficiency considers the entropy generation of the system, it provides deeper insight into the real efficiency of the evaluated machinery. According to the exergy evaluation, the low-duty turbo compressor is not efficient machinery in the lower running zones, where it adjusts the flow rate only using inlet guide vanes. The efficiency in that range drops to 4.08%, and this operating zone is to be avoided as the consumption of power is very high compared to the given output. The best measured exergy efficiency of the turbo compressor was 28.51%.

According to this short overview of the cargo temperature maintenance, it would be ideal to maintain the vessel at a speed at which the LNG vaporizer is not required and where the low-duty turbo compressor maintains the cargo tank pressure and the temperature with the mass flow rate. The energy that is recovered with the evaporated gas inside the boiler varies from 76.2% to 85.8% of the total energy delivered to the main boilers; the rest is sent to the heavy fuel oil (HFO) in dual mode burning. The electric and steam heat power are higher when the low-duty (LD) turbo compressor is

running compared to the running mode in HFO due to the aggregate state of the gas, its transport, and heating the main boilers. The total energy consumption in the boilers is less compared to HFO-only, as LNG has a higher calorific value than HFO.

No data were available from the manufacturer for the running of a turbo compressor at such low temperatures ($-40\text{ }^{\circ}\text{C}$ only). In this study, the turbo compressor was evaluated in the temperature range from -69 to $-105\text{ }^{\circ}\text{C}$, where the compressor was more efficient at lower running speeds due to the increased gas density. In the scientific literature, such analysis is very rare and it brings new light to the running efficiency of the low-duty turbo compressor at different loads in real running conditions. The makers provide the isentropic efficiency of the one running point, but not detailed analysis of the whole running range as presented here. Our recommendation is to maintain the suction temperature of the turbo compressor as low as reasonably possible.

Author Contributions: Data curation, I.P.; Formal analysis, I.P. and V.M.; Investigation, I.P.; Methodology, I.P. and V.M.; Project administration, J.O.; Resources, J.O.; Software, I.G.; Supervision, I.G. and J.O.; Validation, I.G. and J.O.; Visualization, J.O. and V.M.; Writing—original draft, I.P.; Writing—review & editing, I.G. and V.M. All authors have read and agreed to the published version of the manuscript.

Funding: This research was supported by the Croatian Science Foundation under the project IP-2018-01-3739, CEEPUS network CIII-HR-0108, European Regional Development Fund under the grant KK.01.1.1.01.0009 (DATACROSS), project CEKOM under the grant KK.01.2.2.03.0004, University of Rijeka scientific grant uniri-tehnic-18-275-1447, University of Rijeka scientific grant uniri-tehnic-18-18-1146, and University of Rijeka scientific grant uniri-tehnic-18-14.

Conflicts of Interest: The authors declare no conflicts of interest.

Abbreviations

Latin symbols

e	induced EMF, V
$\dot{E}l$	energy rate loss, kW
EMF_{\max}	maximum induced electro motor force, V
ex	specific exergy, kJ/kg
$\dot{E}xd$	exergy destruction rate, kW
f	frequency, Hz
g	gravitational acceleration, m/s^2
h	specific enthalpy, kJ/kg
I	amperage, A
\dot{m}	mass flow rate, kg/h
p	pressure, MPa
P	power, kW
R	specific gas constant, kJ/kgK
\dot{Q}	heat flow rate, kW
\dot{S}	entropy rate, kW/K
t	time, s
T	temperature, K
U	voltage, V
\bar{v}	speed, m/s
v	specific volume, m^3/kg
V	volume, m^3
z	height, m
Z	compressibility factor

Greek symbols

η	efficiency, %
η_{IS}	isentropic efficiency, %
η_I	energy efficiency, %
η_{II}	exergy efficiency, %
φ	power factor
ω	angular velocity, rad/s
θ	angle from reference, radians

Abbreviations

AC	Alternating current
C	Compressor
EMF	electro motor force
HFO	heavy fuel oil
LNG	liquefied natural gas
rpm	revolutions per minute

Subscripts

BOG	boil off gas
CA	compressor actual compressing process
EM	electric motor
IS	isentropic
IN	input
ME	mechanic
OUT	output
m	mixture
i	mixture component

References

- Marques, C.H.; Pereira Belchior, C.R.; Caprace, J.D. An early-stage approach to optimise a marine energy system for liquefied natural gas carriers: Part A—Developed approach. *Ocean Eng.* **2019**, *181*, 161–172. [\[CrossRef\]](#)
- Marques, C.H.; Pereira Belchior, C.R.; Caprace, J.D. An early-stage approach to optimise a marine energy system for liquefied natural gas carriers: Part B—Application. *Ocean Eng.* **2019**, *174*, 96–107. [\[CrossRef\]](#)
- Feng, Y.; Wang, H.; Gao, R.; Zhu, Y. A Zero-Dimensional Mixing Controlled Combustion Model for Real Time Performance Simulation of Marine Two-Stroke Diesel Engines. *Energies* **2019**, *12*, 2000. [\[CrossRef\]](#)
- Raptotasios, S.I.; Sakellariadis, N.F.; Papagiannakis, R.G.; Hountalas, D.T. Application of a multi-zone combustion model to investigate the NOx reduction potential of two-stroke marine diesel engines using EGR. *Appl. Energ.* **2015**, *157*, 814–823. [\[CrossRef\]](#)
- Mrzljak, V.; Medica, V.; Bukovac, O. Volume agglomeration process in quasi-dimensional direct injection diesel engine numerical model. *Energy* **2016**, *115*, 658–667. [\[CrossRef\]](#)
- Ryu, Y.; Lee, Y.; Nam, J. Performance and emission characteristics of additives-enhanced heavy fuel oil in large two-stroke marine diesel engine. *Fuel* **2016**, *182*, 850–856. [\[CrossRef\]](#)
- Senčić, T.; Mrzljak, V.; Blečić, P.; Bonefačić, I. 2D CFD Simulation of Water Injection Strategies in a Large Marine Engine. *J. Mar. Sci. Eng.* **2019**, *7*, 296. [\[CrossRef\]](#)
- Ahn, J.; Noh, Y.; Park, S.H.; Choi, B.I.; Chang, D. Fuzzy-based failure mode and effect analysis (FMEA) of a hybrid molten carbonate fuel cell (MCFC) and gas turbine system for marine propulsion. *J. Power Sources* **2017**, *364*, 226–233. [\[CrossRef\]](#)
- Lorencin, I.; Anđelić, N.; Mrzljak, V.; Car, Z. Multilayer perceptron approach to condition-based maintenance of marine CODLAG propulsion system components. *J. Mar. Res.* **2019**, *33*, 181–190. [\[CrossRef\]](#)
- Ammar, N.R. Environmental and cost-effectiveness comparison of dual fuel propulsion options for emissions reduction onboard LNG carriers. *Shipbuilding* **2019**, *70*, 61–77. [\[CrossRef\]](#)
- Fernández, I.A.; Gómez, M.R.; Gómez, J.R.; Insua, A.A.B. Review of propulsion systems on LNG carriers. *Renew. Sust. Energ. Rev.* **2017**, *67*, 1395–1411. [\[CrossRef\]](#)

12. Budiyanto, M.A.; Nasruddin; Nawara, R. The optimization of exergoenvironmental factors in the combined gas turbine cycle and carbon dioxide cascade to generate power in LNG tanker ship. *Energy Convers. Manag.* **2020**, *205*, 112468. [[CrossRef](#)]
13. Koroglu, T.; Sogut, O.S. Conventional and advanced exergy analyses of a marine steam power plant. *Energy* **2018**, *163*, 392–403. [[CrossRef](#)]
14. Mrzljak, V.; Poljak, I.; Mrakovčić, T. Energy and exergy analysis of the turbo-generators and steam turbine for the main feed water pump drive on LNG carrier. *Energy Convers. Manag.* **2017**, *140*, 307–323. [[CrossRef](#)]
15. Marques, C.H.; Caprace, J.D.; Belchior, C.R.P.; Martini, A. An Approach for Predicting the Specific Fuel Consumption of Dual-Fuel Two-Stroke Marine Engines. *J. Mar. Sci. Eng.* **2019**, *7*, 20. [[CrossRef](#)]
16. Jeong, B.; Oguz, E.; Wang, H.; Zhou, P. Multi-criteria decision-making for marine propulsion: Hybrid, diesel electric and diesel mechanical systems from cost-environment-risk perspectives. *Appl. Energy* **2018**, *230*, 1065–1081. [[CrossRef](#)]
17. Marty, P.; Hétet, J.-F.; Chalet, D.; Corrigan, P. Exergy Analysis of Complex Ship Energy Systems. *Entropy* **2016**, *18*, 127. [[CrossRef](#)]
18. Jeong, B.; Wang, H.; Oguz, E.; Zhou, P. An effective framework for life cycle and cost assessment for marine vessels aiming to select optimal propulsion systems. *J. Clean. Prod.* **2018**, *187*, 111–130. [[CrossRef](#)]
19. Behrendt, C.; Stoyanov, R. Operational characteristic of selected marine turbounits powered by steam from auxiliary oil-fired boilers. *New Trend. Prod. Eng.* **2018**, *1*, 495–501. [[CrossRef](#)]
20. Baldi, F.; Ahlgren, F.; Van Nguyen, T.; Thern, M.; Andersson, K. Energy and Exergy Analysis of a Cruise Ship. *Energies* **2018**, *11*, 2508. [[CrossRef](#)]
21. Ibrahim, T.K.; Basrawi, F.; Awad, O.I.; Abdullah, A.N.; Najafi, G.; Mamat, R.; Hagos, F.Y. Thermal performance of gas turbine power plant based on exergy analysis. *Appl. Therm. Eng.* **2017**, *115*, 977–985. [[CrossRef](#)]
22. Wang, Z.; Li, J.; Fan, K.; Li, S. The Off-Design Performance Simulation of Marine Gas Turbine Based on Optimum Scheduling of Variable Stator Vanes. *Math. Probl. Eng.* **2017**, 2671251. [[CrossRef](#)]
23. Sohret, Y.; Açikkalp, E.; Hepbasli, A.; Karakoc, T.H. Advanced exergy analysis of an aircraft gas turbine engine: Splitting exergy destructions into parts. *Energy* **2015**, *90*, 1219–1228. [[CrossRef](#)]
24. Ibrahim, T.K.; Mohammed, M.K.; Awad, O.I.; Abdalla, A.N.; Basrawi, F.; Mohammed, M.N.; Najafi, G.; Mamat, R. A comprehensive review on the exergy analysis of combined cycle power plants. *Renew. Sust. Energy Rev.* **2018**, *90*, 835–850. [[CrossRef](#)]
25. Lorencin, I.; Anđelić, N.; Mrzljak, V.; Car, Z. Genetic algorithm approach to design of multi-layer perceptron for combined cycle power plant electrical power output estimation. *Energies* **2019**, *12*, 4352. [[CrossRef](#)]
26. Calise, F.; d'Accadia, M.D.; Libertini, L.; Vicidomini, M. Thermoeconomic analysis of an integrated solar combined cycle power plant. *Energy Convers. Manag.* **2018**, *171*, 1038–1051. [[CrossRef](#)]
27. Hou, S.; Wu, Y.; Zhou, Y.; Yu, L. Performance analysis of the combined supercritical CO₂ recompression and regenerative cycle used in waste heat recovery of marine gas turbine. *Energy Convers. Manag.* **2017**, *151*, 73–85. [[CrossRef](#)]
28. Altosole, M.; Benvenuto, G.; Campora, U.; Laviola, M.; Trucco, A. Waste Heat Recovery from Marine Gas Turbines and Diesel Engines. *Energies* **2017**, *10*, 718. [[CrossRef](#)]
29. Boyce, M.P. *Gas Turbine Engineering Handbook*, 4th ed.; Butterworth-Heinemann: Oxford, UK, 2012; pp. 253–355.
30. El-Sayed, A.F. *Aircraft Propulsion and Gas Turbine Engines*, 2nd ed.; CRC Press: Boca Raton, FL, USA, 2017; pp. 839–1034.
31. Giampaolo, T. *Gas Turbine Handbook: Principles and Practice*, 5th ed.; Taylor & Francis: London, UK, 2014; pp. 231–277.
32. Saravanamuttoo, H.I.H.; Rogers, G.F.C.; Cohen, H.; Straznicky, P.V.; Nix, A.C. *Gas Turbine Theory*, 7th ed.; Pearson Education Limited: Harlow, UK, 2017; pp. 154–262.
33. Schobeiri, M.T. *Gas Turbine Design, Components and System Design Integration*; Springer International Publishing: Cham, Switzerland, 2018; pp. 129–211, 369–422. [[CrossRef](#)]
34. Yin, L.; Ju, Y.L. Comparison and analysis of two nitrogen expansion cycles for BOG Re-liquefaction systems for small LNG ships. *Energy* **2019**, *172*, 769–776. [[CrossRef](#)]
35. Tan, H.; Shan, S.; Nie, Y.; Zhao, Q. A new boil-off gas re-liquefaction system for LNG carriers based on dual mixed refrigerant cycle. *Cryogenics* **2018**, *92*, 84–92. [[CrossRef](#)]

36. Poljak, I.; Orović, J.; Mrzljak, V.; Bernečić, D. Energy and Exergy Evaluation of a Two-Stage Axial Vapour Compressor on the LNG Carrier. *Entropy* **2020**, *22*, 115. [CrossRef]
37. Krikkis, R.N. A thermodynamic and heat transfer model for LNG ageing during ship transportation. Towards an efficient boil-off gas management. *Cryogenics* **2018**, *92*, 76–83. [CrossRef]
38. Koo, J.; Oh, S.-R.; Choi, Y.-U.; Jung, J.-H.; Park, K. Optimization of an Organic Rankine Cycle System for an LNG-Powered Ship. *Energies* **2019**, *12*, 1933. [CrossRef]
39. Mrzljak, V.; Poljak, I.; Medica-Viola, V. Dual fuel consumption and efficiency of marine steam generators for the propulsion of LNG carrier. *Appl. Therm. Eng.* **2017**, *119*, 331–346. [CrossRef]
40. Poljak, I.; Orović, J.; Knežević, V.; Vulić, J. The Low Duty Centrifugal Compressor Control System and its Impact on the Surge Pressure. *J. Mari. Transp. Sci.* **2019**, *57*, 47–55. [CrossRef]
41. Hermann, M.; Allheily, L. *Installation, Operation and Maintenance Manual*; Cryostar SAS; Singapore PTE LTD: Singapore, 2004; p. 31.
42. Rosemount™ 2088, 2090P, and 2090F Pressure Transmitters, with HART® and 1-5Vdc Low Power Protocol, Reference Manual 00809-0100-4108, Rev CB November 2017, Emerson. Available online: <https://www.emerson.com/documents/automation/manual-rosemount-2088-2090p-2090f-pressure-transmitters-hart-1-5vdc-low-power-protocol-en-76794.pdf> (accessed on 9 February 2020).
43. Pretrans 5111, Universal Transmitter, Prelectronics. Available online: <http://www.proseskontrol.com/Resimler/Pdf/Raya/5111uk.pdf> (accessed on 9 February 2020).
44. ST3000 ACE Smart Transmitter, JTD Series of Differential Pressure Transmitter, No SS2-DST100-0100 (Rev.6) Yamatake. Available online: http://www.krtproduct.com/krt_Picture/sample/1_spare%20part/yamatake/Fi_ss01/SS2-DST100-0100.pdf (accessed on 9 February 2020).
45. Ship Performance Monitoring/Shaft Power Meter (KYMA). Available online: <https://www.igiantech.com/new-equipment/ship-performance-monitoring/> (accessed on 9 February 2020).
46. *Calculation of BTU Quantity for Delivered LNG*; Loading Port Documentation: Arzew, Algeria, 2014.
47. HIMAP & HICAM, Motor Protection Relay HIMAP-M, Hyundai Heavy Industries. Available online: http://www.tekhar.com/Programma/HYUNDAI/pdf_pict/Ships_pruduction/Himap/HIMAP+HICAM.pdf (accessed on 11 April 2020).
48. Moran, M.J.; Shapiro, H.N.; Boettner, D.D.; Bailey, M.B. *Fundamentals of Engineering Thermodynamics*, 9th ed.; John Wiley & Sons: Hoboken, NJ, USA, 2018; pp. 106–143.
49. Cengel, Y.A.; Boles, M.A.; Kangolu, M. *Thermodynamics an Engineering Approach*, 9th ed.; McGraw-Hill Education: New York, NY, USA, 2019; pp. 211–248.
50. Poljak, I.; Orović, J.; Mrzljak, V. Energy and exergy analysis of the condensate pump during internal leakage from the marine steam propulsion system. *Sci. J. Marit. Res.* **2018**, *32*, 268–280. [CrossRef]
51. Mrzljak, V.; Blečić, P.; Anđelić, N.; Lorencin, I. Energy and exergy analyses of forced draft fan for marine steam propulsion system during load change. *J. Mar. Sci. Eng.* **2019**, *7*, 381. [CrossRef]
52. Mohtaram, S.; Chen, W.; Zargar, T.; Lin, J. Energy-exergy analysis of compressor pressure ratio effects on thermodynamic performance of ammonia water combined cycle. *Energy Convers. Manag.* **2017**, *34*, 77–87. [CrossRef]
53. Kanoglu, M.; Cengel, Y.A.; Dincer, I. *Efficiency Evaluation of Energy Systems*; Springer: Berlin, Germany, 2012; pp. 9–40. [CrossRef]
54. Kaushik, S.C.; Reddy, V.S.; Tyagi, S.K. Energy and exergy analyses of thermal power plants: A review. *Renew. Sust. Energ. Rev.* **2011**, *15*, 1857–1872. [CrossRef]
55. Integrated Publishing's Educational Archive, AC Generation Analysis, Basic AC Theory. Available online: <http://nuclearpowertraining.tpub.com/h1011v3/css/Voltage-Calculations-29.html> (accessed on 7 April 2020).
56. Chen, W.K. *The Electrical Engineering Handbook*; Academic Press: Oxford, UK, 2005; p. 810.
57. Gussov, M. *Basic Electricity*, 2nd ed.; Schaum's Outline Series; The McGraw-Hill Companies: New York, NY, USA, 2007; pp. 477–482.
58. Mateu-Royoa, C.; Navarro-Esbría, J.; Mota-Babilonia, A.; Molés, F.; Amat-Albuixech, M. Experimental exergy and energy analysis of a novel high-temperature heat pump with scroll compressor for waste heat recovery. *Appl. Energy* **2019**, *253*, 113504. [CrossRef]
59. Orović, J.; Mrzljak, V.; Poljak, I. Efficiency and Losses Analysis of Steam Air Heater from Marine Steam Propulsion Plant. *Energies* **2018**, *11*, 3019. [CrossRef]

60. Ranjbar, F.; Chitsaz, A.; Mahmoudi, S.M.S.; Khalilarya, S.; Rosen, M.A. Energy and exergy assessments of a novel trigeneration system based on a solid oxide fuel cell. *Energy Convers. Manag.* **2014**, *87*, 318–327. [[CrossRef](#)]
61. Lorencin, I.; Anđelić, N.; Mrzljak, V.; Car, Z. Exergy analysis of marine steam turbine labyrinth (gland) seals. *J. Mar. Res.* **2019**, *33*, 76–83. [[CrossRef](#)]
62. Zare, V.; Hasanzadeh, M. Energy and exergy analysis of a closed Brayton cycle-based combined cycle for solar power tower plants. *Energy Convers. Manag.* **2016**, *128*, 227–237. [[CrossRef](#)]
63. Uysal, C.; Kurt, H.; Kwak, H.Y. Exergetic and thermoeconomic analyses of a coal-fired power plant. *Int. J. Therm. Sci.* **2017**, *117*, 106–120. [[CrossRef](#)]
64. Adibhatla, S.; Kaushik, S.C. Energy and exergy analysis of a super critical thermal power plant at various load conditions under constant and pure sliding pressure operation. *Appl. Ther. Eng.* **2014**, *73*, 49–63. [[CrossRef](#)]
65. Mrzljak, V.; Poljak, I.; Prpić-Oršić, J. Exergy analysis of the main propulsion steam turbine from marine propulsion plant. *Shipbuilding* **2019**, *70*, 59–77. [[CrossRef](#)]
66. Brasz, J.J. Oil-free centrifugal refrigeration compressors: From HFC134a to HFO1234ze(E). In Proceedings of the 8th International Conference on Compressors and Their Systems, London, UK, 9–10 September 2013; Woodhead Publishing: Sawston, Cambridge, UK, 2013; p. 472.
67. Gresh, M.T. *Compressor Performance Aerodynamics for the User*, 2nd ed.; Elsevier Science & Technology Books; Elsevier Inc.: Cambridge, MA, USA, 2001; pp. 55–58.
68. SankeyMATIC. Available online: <http://sankeymatic.com/build> (accessed on 9 February 2020).
69. Lemmon, E.W.; Huber, M.L.; McLinden, M.O. *NIST Reference Fluid Thermodynamic and Transport Properties—REFPROP; Version 9.0; User’s Guide*; The National Institute of Standards and Technology: Boulder, CO, USA, 2010.
70. Cao, J.; Zhang, X.; Yang, G.; Zou, X. Robust Control of Pressure for LNG Carrier Cargo Handling System via Mirror-Mapping Approach. *Hindawi Complex.* **2018**, 7465391. [[CrossRef](#)]
71. Gaganis, V.; Homouz, D.; Maalouf, M.; Khoury, N.; Polychronopoulou, K. An Efficient Method to Predict Compressibility Factor of Natural Gas Streams. *Energies* **2019**, *12*, 2577. [[CrossRef](#)]
72. Rogers, W.S.; Cox, D.J. Increased Cargo Tank Filling Limits on LNG Carriers—The LR Approach. Available online: <http://www.ivt.ntnu.no/ept/fag/tep4215/innhold/LNG%20Conferences/1998/Papers/6-3-Rogers.PDF> (accessed on 11 April 2020).
73. Liquefied Gas Carrier, Safety and Operational Limit. Available online: <http://www.liquefiedgascarrier.com/slashing.html> (accessed on 11 April 2020).
74. Ahmed, T. *Natural Gas Properties, Equations of State and PVT Analysis*; Gulf Publishing Company: Houston, TX, USA, 2007; pp. 136–158.
75. Modern LNG Carrier Technology—Technology Report#05—Autumn 2019, Bureau Veritas Marine & Offshore 8 Cours du Triangle 92937 Paris-La Défense, France. Available online: https://www.bureauveritas.jp/news/pdf/BV_Technology%20Report_Modern%20LNG_Web_Planche.pdf (accessed on 11 April 2020).



© 2020 by the authors. Licensee MDPI, Basel, Switzerland. This article is an open access article distributed under the terms and conditions of the Creative Commons Attribution (CC BY) license (<http://creativecommons.org/licenses/by/4.0/>).